A broadband 2 × 2 multimode interference coupler for mid-infrared wavelengths

CALLUM J. STIRLING[1,*], ROBERT HALIR[2], ALEJANDRO SÁNCHEZ-POSTIGO[2], ZHIBO QU[1], JAMIE D. REYNOLDS[1], JORDI SOLER PENADÉS[3], GANAPATHY SENTHIL MURUGAN[1], ALEJANDRO ORTEGA-MOÑUX[2], J. GONZALO WANGÜEMERT-PÉREZ[2], ÍÑIGO MOLINA-FERNÁNDEZ[2], GORAN Z. MASHANOVICH[1,4], AND MILOS NEDELJKOVIC[1]

[1] *Optoelectronics Research Centre, Zepler Institute for Photonics and Nanoelectronics, University of Southampton, Southampton, SO17 1BJ, UK*
[2] *Telecommunication Research Institute (TELMA), Universidad de Málaga, CEI Andalucía TECH, Louis Pasteur 35, 29010 Málaga (Spain)*
[3] *VLC Photonics, Building 9B, Universidad de Politécnica de Valencia, Camino de Vera s/n, 46022 Valencia, Spain*
[4] *School of Electrical Engineering, University of Belgrade, 11120 Belgrade, Serbia*
[*] *Corresponding author: c.stirling@soton.ac.uk*

Compiled October 15, 2021

Beamsplitters are core components of photonic integrated circuits and are often implemented with multimode interference couplers. While these devices offer high performance, their operational bandwidth is still restrictive for sensing applications in the mid-infrared wavelength range. Here we experimentally demonstrate a subwavelength-structured 2 × 2 multimode interference coupler with high performance in the 3.1 − 3.7 μm range, doubling the bandwidth of a conventional device.

http://dx.doi.org/10.1364/ao.XX.XXXXXX

The mid-infrared (MIR) wavelength region of 2 − 20 μm is attractive for group IV photonics, as integrated sensors could take advantage of the characteristic spectral absorption lines that many chemicals exhibit in this region due to molecular vibrations [1]. Group IV waveguides with low propagation losses have been shown at MIR wavelengths [2–5], and absorption spectroscopy sensing has been demonstrated for specific applications [6–8]. A photonic sensor with a wide optical bandwidth would be advantageous as the device could be used for multiple applications without redesign, enabling high-volume and low-cost production. Furthermore, broader transmission spectra can provide sensitivity to the absorption features of multiple analytes (enabling differentiation of analytes), or provide more information about an unknown analyte by investigating broad peaks or multiple absorptions. Consequently, the photonic integrated circuit and its constituent components need a wide working bandwidth. The beamsplitter is a key example of such a component since it is necessary for any integrated photonic circuit beyond a minimal complexity. For example, in a sensing application, they are used to split light between sensing and reference arms, or to split light into multiple channels for a Fourier transform spectrometer [9].

Y-splitters offer a bandwidth equal to the operable wavelength range of the waveguide, but their idealised infinitely small tips at the centre of the splitter are intolerant to fabrication error, which can increase insertion loss and imbalance [10]. Likewise, small tip sizes are required for adiabatic power splitters, that have been shown to exhibit low insertion losses over a 230 nm bandwidth around a central wavelength of 3.8 μm [11]. Further, both of these splitter types are symmetrical 1 × 2 splitters, so they cannot be used to construct devices such as Mach-Zehnder interferometer (MZI) switches. Directional couplers have a 2 × 2 configuration and can thus be used for switches. However, the coupling ratio is wavelength-dependent and gives imbalanced outputs over a broad wavelength range [12, 13]. Although this can be mitigated by controlling the waveguide dispersion, achieving a 85 nm bandwidth around 3.8 μm [14], this is insufficient for the sensing applications.

Multimode interferometers (MMIs) are commonly used for beamsplitting, due to their fabrication tolerance and low insertion losses. However, MMIs inherently have a limited bandwidth [15], which needs to be addressed for broadband circuits. The graded-index SiGe platform has enabled MMIs with bandwidths approaching an octave of frequency at longer MIR wavelengths, experimentally demonstrated with sub-1 dB insertion loss over a 3 μm bandwidth at 7 μm [16] and a similar simulated loss over 7.5 − 12.5 μm [17]. However, this approach relies on the dispersion of the SiGe material itself, so it is not applicable to other waveguide types, and results in a comparatively large footprint. Suspended silicon MMIs with a subwavelength cladding have been demonstrated with up to 200 nm bandwidth at 3.8 μm, but this device is expected to still have a strong wavelength dependence as it is based on a conventional design [18, 19]. Tunable graphene-based plasmonic MMIs offer low imbalance over a 2 μm bandwidth with a compact footprint, but suffer from high insertion loss and a complicated fabrication process [20, 21].

Alternatively, broadening the working bandwidth of splitters can be achieved on silicon-on-insulator (SOI) using subwavelength features [22, 23]. Subwavelength structures have been used to make fabrication-tolerant near-infrared (NIR) Y-junctions [24], directional couplers with a 175 nm bandwidth

around 3.8 μm [25], polarization splitters in both the NIR and MIR [26, 27], and increase the compactness and bandwidth of MMIs in the NIR [28, 29]. In this work, we use a subwavelength grating (SWG) in the multimode region to achieve an MMI, shown in Fig. 1, with 52 μm × 8 μm device footprint (including waveguide tapers) and broadband performance over 600 nm around 3.4 μm, that can be fabricated in a single etch.

In the SWG-MMI, the multimode region (with length L_{MMI}) is composed of an array of air-clad silicon strips (each with length a) oriented along the x-direction, with thickness $h = 500$ nm and width W_{MMI} (see Fig. 1). The pitch of this array, Λ, is smaller than the wavelength of light propagating through the structure, which thus behaves as an equivalent homogeneous, anisotropic metamaterial. For a given pitch, the duty cycle, a/Λ, is fixed at 50% as this maximizes the length of the strips and the gaps between them, thereby facilitating fabrication. When light is launched into the multimode region, it excites several guided modes, which interfere as they propagate, forming images of the input at distances governed by the beat length L_π, given by [29]

$$L_\pi = \frac{\pi}{\beta_0 - \beta_1} \approx \frac{4W_{\mathrm{MMI}}^2}{3\lambda}\frac{n_{zz}^2}{n_{xx}}, \quad (1)$$

where β_0 and β_1 are the propagation constants of the lowest order Floquet modes of the multimode region, λ is the free-space wavelength, and n_{zz}, n_{xx} are the equivalent metamaterial indices in the z- and x-directions respectively. Compared to a conventional MMI, in which $n_{zz} = n_{xx}$ for the core material index, the factor n_{zz}^2/n_{xx} reduces the beat length approximately twofold, yielding a shorter device and, since the wavelength-dependence of $L_\pi$is proportional to n_{zz}^2/n_{xx}, an increased bandwidth. By designing the pitch, the dispersion of the SWG can be tuned to further enhance the bandwidth (see Fig. 3 in [29]).

We initiated the design with the MMI width $W_{\mathrm{MMI}} = 8$ μm and the subwavelength access waveguides with width $w_A = 3.1$μm. These wide access waveguides minimize power loss when coupling into the multimode region. Via Floquet-mode simulation we found that the pitch that resulted in the smallest variation of the beat length over the wavelength range of interest ($3 - 4$ μm) is $\Lambda \sim 465$ nm. We then set the center-to-center separation of the input/output waveguides to $s = 5.1$ μm so as to have negligible coupling between them over a distance of several tens of microns. The interconnecting $w_I = 1.1$ μm wide single mode waveguides have to be converted to subwavelength-structured waveguides - this is achieved by a $L_T \sim 13$ μm long "inversed" taper with the same SWG period and duty cycle as the multimode region, as shown in Fig. 1 (the decrease in strip waveguide width and increase in SWG segment width are both linear along the taper length). The width and length of the multimode region were then iteratively optimized, yielding $W_{\mathrm{MMI}} = 7.7$ μm and 52 periods ($L_{\mathrm{MMI}} \sim 24.2$ μm). The simulated performance of this device is shown in Fig. 2. If the field overlap with the fundamental waveguide mode at each of the MMI outputs is A and B respectively, then the MMI imbalance (in dB) is $10\log_{10}(|A|^2/|B|^2)$ and its insertion loss (in dB) is $-10\log_{10}(|A|^2 + |B|^2)$. For a 50:50 beamsplitter with no imbalance or insertion loss, $A = B = 1/\sqrt{2}$. The phase error, θ_{err}, is defined as the deviation of the phase difference between the outputs, θ, from its ideal value ($\theta = \pi/2$). Using these metrics, the designed SWG-MMI shows excellent simulated performance in the $3 - 4$ μm wavelength range (see Fig. 2).

To experimentally verify the bandwidth enhancements of the SWG-MMIs, a series of devices were embedded in asymmetric

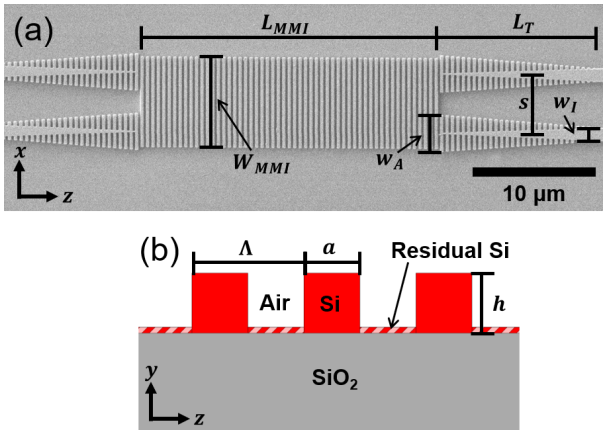

Fig. 1. (a) SEM micrograph of a fabricated SWG-MMI for MIR wavelengths. (b) Schematic longitudinal cross-section of the multimode region, showing the unintended residual silicon layer that can remain between subwavelength features.

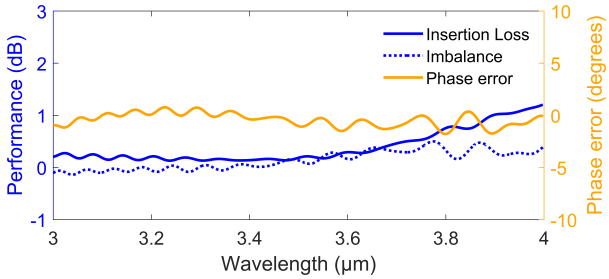

Fig. 2. Simulated performance of the SWG-MMI with optimal dimensions: no residual silicon layer, $W_{\mathrm{MMI}} = 7.7$ μm, 50% duty-cycle and 52 periods.

MZIs with an arm length difference of 20 μm and fabricated on an SOI chip. The normalised transmission spectrum of an asymmetric MZI can be modelled analytically; by fitting this model to the experimentally measured spectra, an estimation of the MMI performance (imbalance, insertion loss, and phase error) can be calculated [30]. Note that the phase error of the MMIs can only be obtained by using MZIs. For comparison, similar MZIs based on conventional MMIs (centred at $\lambda = 3.4$ μm) were also fabricated. Designs with variations of the critical parameters, i.e. the number of periods and the duty cycle of the SWG, around the simulated optimal values were included. Straight waveguides were used to obtain a coupling loss reference.

The design was transferred to the sample using ZEP-520A photoresist and a JEOL JBX-9300FS electron beam lithography tool, before etching in an Oxford Instruments ICP 380 plasma system. The sides of the chip were polished to expose the waveguide end facets, for broadband fiber-to-chip butt coupling. Fig. 1(a) shows a scanning electron microscope (SEM) image of the best-performing device, after completed fabrication.

The MZI test structures were characterised using an M-Squared tunable optical parametric oscillator (with manufacturer-specified linewidth of <10 cm^{-1}); the upper wavelength limit of the source prevented measurements beyond 3.7 μm. The laser was coupled into a single-mode fiber using a ZnSe lens for butt-coupling into the chip. The output was coupled into a multimode fiber and a Vigo System HgCdTe detector was used to collect power from the fiber. A lock-in amplifier was used for signal recovery and a half-wave plate

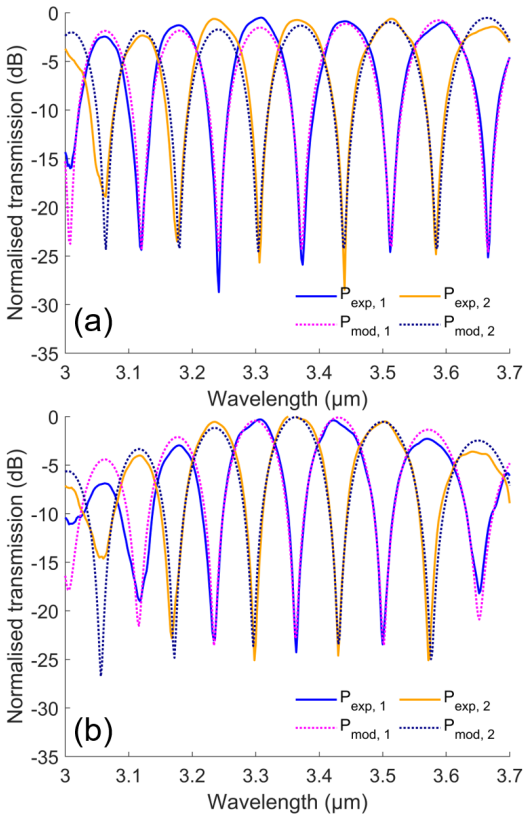

Fig. 3. MZI transmission spectrum and the fitted model, for (a) the SWG-MMI and (b) the conventional MMI. $P_{\text{exp},1}$ and $P_{\text{exp},2}$ are the experimentally measured outputs of the MZI; $P_{\text{mod},1}$ and $P_{\text{mod},2}$ are the fitted model for each output. For both (a) and (b), the noise floor has been subtracted from the experimental data.

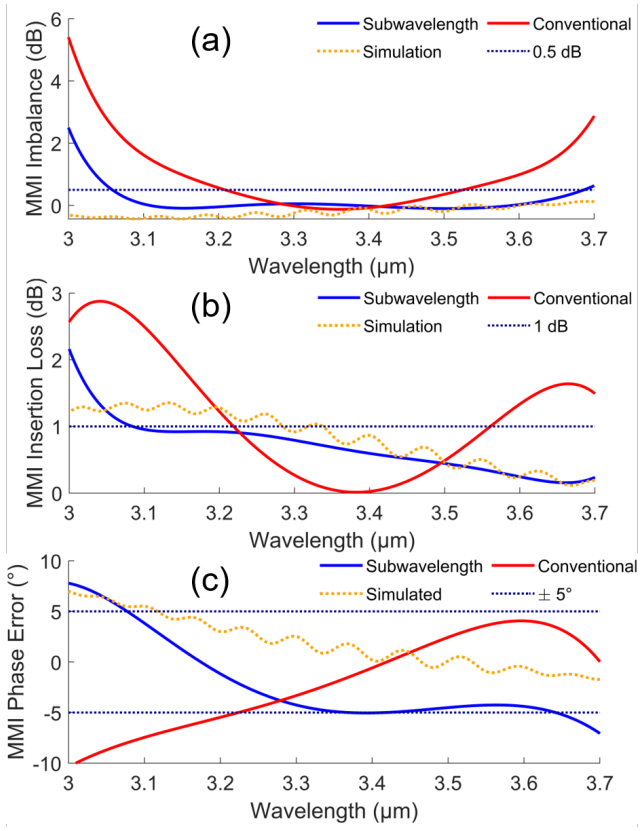

Fig. 4. (a) The imbalance; (b) insertion loss; and (c) phase error of the SWG and conventional MMIs calculated from the measured MZI transmission spectra. The simulated MMI uses the estimated fabricated dimensions: a 15 nm residual silicon layer, $W_{\text{MMI}} = 7.6\,\mu\text{m}$, 55% duty cycle and 55 periods.

was placed in the input beam path for polarization control. A FLIR infrared camera was used for fibre-waveguide facet alignment.

The measured transmission through the unbalanced MZIs composed of SWG-based and conventional MMIs is shown in Figs. 3 (a) and (b). For $\lambda < 3.2\,\mu\text{m}$, the detector noise floor relative to the laser power limited the measurement of the extinction, so the noise floor was subtracted in this region. The noise floor spectrum was estimated by measuring the lock-in amplifier output with no input power, and then dividing that value by the output of the lock-in amplifier when measuring the transmission spectrum of the normalization waveguide.

From Fig. 3 the MZI using the SWG-MMIs exhibits higher transmission peaks and stronger extinction compared to the MZI with conventional MMIs, indicating improved insertion loss and imbalance. To evaluate the performance of individual MMIs, the measured spectra were fitted to an analytical model. The modelled output powers, $P_{\text{mod},1}$ and $P_{\text{mod},2}$, of a 2×2 asymmetric MZI with path difference ΔL between its arms are

$$\begin{bmatrix} P_{\text{mod},1} \\ P_{\text{mod},2} \end{bmatrix} = \begin{bmatrix} A^4 + B^4 + 2A^2B^2\cos(\beta\Delta L - 2\theta) \\ 2A^2B^2[1 + \cos(\beta\Delta L)] \end{bmatrix} \quad \textbf{(2)}$$

with propagation constant β for the MZI arm waveguide mode. The full derivation of Eq. 2 is shown in Supplement 1.

The difference between an ideal MMI and an actual device is considered by introducing wavelength-dependent errors to the MMI outputs for the field amplitudes, $A_{\text{err}}(\lambda)$ and $B_{\text{err}}(\lambda)$, and the phase difference, $\theta_{\text{err}}(\lambda)$, so that $A(\lambda) = 1/\sqrt{2} + A_{\text{err}}(\lambda)$, $B(\lambda) = 1/\sqrt{2} + B_{\text{err}}$ and $\theta(\lambda) = \pi/2 + \theta_{\text{err}}(\lambda)$. The MZI transmission spectrum, the imbalance, insertion loss and phase error can then be calculated from the errors. Therefore, by fitting the MZI output powers from the analytical model, $P_{\text{mod},1}$ and $P_{\text{mod},2}$, to the experimentally measured MZI spectra, $P_{\text{exp},1}$ and $P_{\text{exp},2}$ by varying the error parameters, the MMI performance can be found. To balance accuracy without overfitting, each error parameter was fitted as a 6^{th}-order polynomial, using a genetic algorithm to minimise the difference between the measured and modelled spectra. Finally, to account for the finite linewidth of the source in the measured spectra, $P_{\text{mod},1}$ and $P_{\text{mod},2}$ were convoluted with a Lorentzian function, with full-width at half-maximum equal to a fitted linewidth of $0.7\,\text{cm}^{-1}$. As shown in Fig. 3, this model results in a very good fit of our measurement data. For $\lambda < 3.1\,\mu\text{m}$, the low signal-to-noise ratio limited matching as close as the rest of the spectrum, so the extracted imbalance and insertion loss are overestimated in this range; the low signal-to-noise ratio may be caused by sidelobes of the SWG metamaterial bandgap affecting transmission at shorter wavelengths [31].

The extracted MMI performance parameters (insertion loss, imbalance and phase error) are shown in Fig. 4 for the best device, which has a duty cycle of 55%, a 55 periods long multimode region ($L_{\text{MMI}} \sim 25.6\,\mu\text{m}$) and a $W_{\text{MMI}} = 7.6\,\mu\text{m}$ wide multimode region. These dimensions deviate slightly from the

optimal simulated values. However, the simulation of the optimal device performance (Fig. 2) assumed that there is no residual silicon layer between the subwavelength features. As shown in Fig. 1(b), this thin layer can remain after etching due to the small feature size of the SWG. When a device with the fabricated parameters and a 15 nm residual layer is simulated, we obtain a good match with the measured performance (see Fig. 4).

As the wavelength moves away from the central wavelength, the conventional MMI is quickly outperformed by the SWG-MMI across the spectrum (see Fig. 4). Considering imbalance, the 0.5 dB bandwidth for the subwavelength device (628 nm) is almost double the bandwidth of the conventional one (316 nm). Likewise, for insertion loss, the 1 dB bandwidth for the SWG-MMI (616 nm) is approximately twice that of the conventional MMI (343 nm). The performance difference is less marked for the phase error, but for the SWG-MMI it is roughly constant for $\lambda > 3.4\,\mu$m and less than 5° across most of the spectrum, while for the conventional MMI it changes consistently over the wavelength range: $|\theta_{\text{err}}| < 5^\circ$ for 564 nm of the measured spectrum for the SWG-MMI, compared to 476 nm for the conventional MMI.

In conclusion, we designed an MMI with a subwavelength-structured multimode region with a high performance over the MIR wavelength range of $3-4\,\mu$m. Importantly, this high-performance bandwidth is achieved using devices that have a small footprint and can be fabricated simply, with a single lithography and etch step, on a 500 nm-thick SOI platform. We fabricated this device and, by embedding it in an asymmetric MZI, demonstrated that it exhibits a twofold bandwidth enhancement over a conventional MMI around 3.4 μm, when considering imbalance and insertion loss. This increased bandwidth will be critical for future MIR photonic integrated circuits used for absorption spectroscopy applications.

Funding. Engineering and Physical Sciences Research Council (EPSRC) (EP/N013247/1), Royal Academy of Engineering (RF201617/16/33), Consejería de Economía, Conocimiento, Empresas y Universidad, Junta de Andalucía (P18-RT-793)

Disclosures. The authors declare no conflicts of interest.

Data availability. All data supporting this study are openly available from the University of Southampton repository at https://doi.org/10.5258/SOTON/D1914.

Supplemental document. See Supplement 1 for the full derivation of the analytical model used for the MZI transmission spectrum.

REFERENCES

1. R. Soref, Nat. Photonics **4**, 495 (2010).
2. J. S. Penadés, A. Sánchez-Postigo, M. Nedeljkovic, A. Ortega-Moñux, J. G. Wangüemert-Pérez, Y. Xu, R. Halir, Z. Qu, A. Z. Khokhar, A. Osman, W. Cao, C. G. Littlejohns, P. Cheben, Í. Molina-Fernández, and G. Z. Mashanovich, Opt. Lett. **43**, 795 (2018).
3. K. Gallacher, R. Millar, U. Griškevičiūte, L. Baldassarre, M. Sorel, M. Ortolani, and D. J. Paul, Opt. Express **26**, 25667 (2018).
4. J. M. Ramirez, Q. Liu, V. Vakarin, J. Frigerio, A. Ballabio, X. L. Roux, D. Bouville, L. Vivien, G. Isella, and D. Marris-Morini, Opt. Express **26**, 870 (2018).
5. A. Sánchez-Postigo, A. Ortega-Moñux, J. S. Penadés, A. Osman, M. Nedeljkovic, Z. Qu, Y. Wu, Í. Molina-Fernández, P. Cheben, G. Z. Mashanovich, and J. G. Wangüemert-Pérez, Opt. Express **29**, 16867 (2021).
6. P. T. Lin, V. Singh, J. Hu, K. Richardson, J. D. Musgraves, I. Luzinov, J. Hensley, L. C. Kimerling, and A. Agarwal, Lab Chip **13**, 2161 (2013).
7. C. Ranacher, C. Consani, A. Tortschanoff, R. Jannesari, M. Bergmeister, T. Grille, and B. Jakoby, Sensors Actuators A: Phys. **277**, 117 (2018).
8. V. Mittal, G. Devitt, M. Nedeljkovic, L. G. Carpenter, H. M. H. Chong, J. S. Wilkinson, S. Mahajan, and G. Z. Mashanovich, Biomed. Opt. Express **11**, 4714 (2020).
9. D. M. Kita, B. Miranda, D. Favela, D. Bono, J. Michon, H. Lin, T. Gu, and J. Hu, Nat. Commun. **9** (2018).
10. C. J. Stirling, B. Guilhabert, W. Cao, K. S. Kiang, A. Z. Khokhar, M. Nedeljkovic, M. J. Strain, and G. Z. Mashanovich, Proc. SPIE **11285**, 224 (2020).
11. J. X. B. Sia, W. Wang, X. Guo, J. Zhou, Z. Zhang, M. S. Rouifed, X. Li, Z. L. Qiao, C. Y. Liu, C. Littlejohns, G. T. Reed, and H. Wang, IEEE Photonics J. **11**, 1 (2019).
12. L. Chrostowski and M. Hochberg, *Silicon Photonics Design: From Devices to Systems* (Cambridge University Press, 2015).
13. B. Dong, X. Guo, C. P. Ho, B. Li, H. Wang, C. Lee, X. Luo, and G.-Q. Lo, IEEE Photonics J. **9**, 1 (2017).
14. B. Dong, X. Luo, T. Hu, T. X. Guo, H. Wang, D.-L. Kwong, P. G.-Q. Lo, and C. Lee, IEEE J. Sel. Top. Quantum Electron. **24**, 1 (2018).
15. P. Besse, M. Bachmann, H. Melchior, L. Soldano, and M. Smit, J. Light. Technol. **12**, 1004 (1994).
16. V. Vakarin, J. M. Ramírez, J. Frigerio, A. Ballabio, X. L. Roux, Q. Liu, D. Bouville, L. Vivien, G. Isella, and D. Marris-Morini, Opt. Lett. **42**, 3482 (2017).
17. V. Vakarin, J. M. Ramírez, J. Frigerio, Q. Liu, A. Ballabio, X. Le Roux, C. Alonso-Ramos, G. Isella, P. Cheben, W. N. Ye, L. Vivien, and D. Marris-Morini, Appl. Sci. **8** (2018).
18. J. S. Penadés, A. Ortega-Moñux, M. Nedeljkovic, J. G. Wangüemert-Pérez, R. Halir, A. Z. Khokhar, C. Alonso-Ramos, Z. Qu, I. Molina-Fernández, P. Cheben, and G. Z. Mashanovich, Opt. Express **24**, 22908 (2016).
19. A. Sánchez-Postigo, J. G. Wangüemert-Pérez, J. Soler Penadés, A. Ortega-Moñux, M. Nedeljkovic, R. Halir, F. El Mokhtari Mimun, Y. Xu Cheng, Z. Qu, A. Z. Khokhar, A. Osman, W. Cao, C. G. Littlejohns, P. Cheben, G. Z. Mashanovich, and I. Molina-Fernández, IET Optoelectronics **13**, 55 (2019).
20. R. Zheng, D. Gao, and J. Dong, IEEE Photonics Technol. Lett. **28**, 645 (2016).
21. C.-C. Huang and T.-C. Sun, Sci. Reports **9**, 12756 (2019).
22. P. Cheben, R. Halir, J. H. Schmid, H. A. Atwater, and D. R. Smith, Nature **560**, 565 (2018).
23. R. Halir, A. Ortega-Moñux, D. Benedikovic, G. Z. Mashanovich, J. G. Wangüemert-Pérez, J. H. Schmid, I. Molina-Fernández, and P. Cheben, Proc. IEEE **106**, 2144 (2018).
24. R. Fernández de Cabo, D. González-Andrade, P. Cheben, and A. V. Velasco, Nanomaterials **11** (2021).
25. B. Dong, T. Hu, X. Luo, Y. Chang, X. Guo, H. Wang, D.-L. Kwong, G.-Q. Lo, and C. Lee, Nanomaterials **8**, 893 (2018).
26. A. Herrero-Bermello, J. M. Luque-González, A. V. Velasco, A. Ortega-Moñux, P. Cheben, and R. Halir, IEEE Photonics J. **11**, 1 (2019).
27. T. Hu, M. S. Rouifed, H. Qiu, X. Guo, C. G. Littlejohns, C. Liu, and H. Wang, IEEE Photonics Technol. Lett. **28**, 911 (2016).
28. A. Ortega-Moñux, C. Alonso-Ramos, A. Maese-Novo, R. Halir, L. Zavargo-Peche, D. Pérez-Galacho, I. Molina-Fernández, J. G. Wangüemert-Pérez, P. Cheben, J. H. Schmid, J. Lapointe, D. Xu, and S. Janz, Laser & Photonics Rev. **7**, L12 (2013).
29. R. Halir, P. Cheben, J. M. Luque-González, J. D. Sarmiento-Merenguel, J. H. Schmid, G. Wangüemert-Pérez, D.-X. Xu, S. Wang, A. Ortega-Moñux, and Í. Molina-Fernández, Laser & Photonics Rev. **10**, 1039 (2016).
30. M. A. Tran, T. Komljenovic, J. C. Hulme, M. L. Davenport, and J. E. Bowers, IEEE Photonics Technol. Lett. **28**, 1517 (2016).
31. T. Barwicz, B. Peng, R. Leidy, A. Janta-Polczynski, T. Houghton, M. Khater, S. Kamapurkar, S. Engelmann, P. Fortier, N. Boyer, and W. M. J. Green, IEEE J. Sel. Top. Quantum Electron. **25** (2019).

FULL REFERENCES

1. R. Soref, "Mid-infrared photonics in silicon and germanium," Nat. Photonics **4**, 495–497 (2010).
2. J. S. Penadés, A. Sánchez-Postigo, M. Nedeljkovic, A. Ortega-Moñux, J. G. Wangüemert-Pérez, Y. Xu, R. Halir, Z. Qu, A. Z. Khokhar, A. Osman, W. Cao, C. G. Littlejohns, P. Cheben, Í. Molina-Fernández, and G. Z. Mashanovich, "Suspended silicon waveguides for long-wave infrared wavelengths," Opt. Lett. **43**, 795–798 (2018).
3. K. Gallacher, R. Millar, U. Griškevičiūte, L. Baldassarre, M. Sorel, M. Ortolani, and D. J. Paul, "Low loss Ge-on-Si waveguides operating in the 8-14 μm atmospheric transmission window," Opt. Express **26**, 25667–25675 (2018).
4. J. M. Ramirez, Q. Liu, V. Vakarin, J. Frigerio, A. Ballabio, X. L. Roux, D. Bouville, L. Vivien, G. Isella, and D. Marris-Morini, "Graded SiGe waveguides with broadband low-loss propagation in the mid infrared," Opt. Express **26**, 870–877 (2018).
5. A. Sánchez-Postigo, A. Ortega-Moñux, J. S. Penadés, A. Osman, M. Nedeljkovic, Z. Qu, Y. Wu, Í. Molina-Fernández, P. Cheben, G. Z. Mashanovich, and J. G. Wangüemert-Pérez, "Suspended germanium waveguides with subwavelength-grating metamaterial cladding for the mid-infrared band," Opt. Express **29**, 16867–16878 (2021).
6. P. T. Lin, V. Singh, J. Hu, K. Richardson, J. D. Musgraves, I. Luzinov, J. Hensley, L. C. Kimerling, and A. Agarwal, "Chip-scale mid-infrared chemical sensors using air-clad pedestal silicon waveguides," Lab Chip **13**, 2161–2166 (2013).
7. C. Ranacher, C. Consani, A. Tortschanoff, R. Jannesari, M. Bergmeister, T. Grille, and B. Jakoby, "Mid-infrared absorption gas sensing using a silicon strip waveguide," Sensors Actuators A: Phys. **277**, 117–123 (2018).
8. V. Mittal, G. Devitt, M. Nedeljkovic, L. G. Carpenter, H. M. H. Chong, J. S. Wilkinson, S. Mahajan, and G. Z. Mashanovich, "Ge on Si waveguide mid-infrared absorption spectroscopy of proteins and their aggregates," Biomed. Opt. Express **11**, 4714–4722 (2020).
9. D. M. Kita, B. Miranda, D. Favela, D. Bono, J. Michon, H. Lin, T. Gu, and J. Hu, "High-performance and scalable on-chip digital Fourier transform spectroscopy," Nat. Commun. **9** (2018).
10. C. J. Stirling, B. Guilhabert, W. Cao, K. S. Kiang, A. Z. Khokhar, M. Nedeljkovic, M. J. Strain, and G. Z. Mashanovich, "Investigations into group IV photonic waveguides with a wide working optical bandwidth," Proc. SPIE **11285**, 224 – 233 (2020).
11. J. X. B. Sia, W. Wang, X. Guo, J. Zhou, Z. Zhang, M. S. Rouifed, X. Li, Z. L. Qiao, C. Y. Liu, C. Littlejohns, G. T. Reed, and H. Wang, "Mid-infrared, ultra-broadband, low-loss, compact arbitrary power splitter based on adiabatic mode evolution," IEEE Photonics J. **11**, 1–11 (2019).
12. L. Chrostowski and M. Hochberg, *Silicon Photonics Design: From Devices to Systems* (Cambridge University Press, 2015).
13. B. Dong, X. Guo, C. P. Ho, B. Li, H. Wang, C. Lee, X. Luo, and G.-Q. Lo, "Silicon-on-insulator waveguide devices for broadband mid-infrared photonics," IEEE Photonics J. **9**, 1–10 (2017).
14. B. Dong, X. Luo, T. Hu, T. X. Guo, H. Wang, D.-L. Kwong, P. G.-Q. Lo, and C. Lee, "Compact low loss mid-infrared wavelength-flattened directional coupler (WFDC) for arbitrary power splitting ratio enabled by rib waveguide dispersion engineering," IEEE J. Sel. Top. Quantum Electron. **24**, 1–8 (2018).
15. P. Besse, M. Bachmann, H. Melchior, L. Soldano, and M. Smit, "Optical bandwidth and fabrication tolerances of multimode interference couplers," J. Light. Technol. **12**, 1004–1009 (1994).
16. V. Vakarin, J. M. Ramírez, J. Frigerio, A. Ballabio, X. L. Roux, Q. Liu, D. Bouville, L. Vivien, G. Isella, and D. Marris-Morini, "Ultra-wideband Ge-rich silicon germanium integrated Mach-Zehnder interferometer for mid-infrared spectroscopy," Opt. Lett. **42**, 3482–3485 (2017).
17. V. Vakarin, J. M. Ramírez, J. Frigerio, Q. Liu, A. Ballabio, X. Le Roux, C. Alonso-Ramos, G. Isella, P. Cheben, W. N. Ye, L. Vivien, and D. Marris-Morini, "Wideband ge-rich sige polarization-insensitive waveguides for mid-infrared free-space communications," Appl. Sci. **8** (2018).
18. J. S. Penadés, A. Ortega-Moñux, M. Nedeljkovic, J. G. Wangüemert-Pérez, R. Halir, A. Z. Khokhar, C. Alonso-Ramos, Z. Qu, I. Molina-Fernández, P. Cheben, and G. Z. Mashanovich, "Suspended silicon mid-infrared waveguide devices with subwavelength grating metamaterial cladding," Opt. Express **24**, 22908–22916 (2016).
19. A. Sánchez-Postigo, J. G. Wangüemert-Pérez, J. Soler Penadés, A. Ortega-Moñux, M. Nedeljkovic, R. Halir, F. El Mokhtari Mimun, Y. Xu Cheng, Z. Qu, A. Z. Khokhar, A. Osman, W. Cao, C. G. Littlejohns, P. Cheben, G. Z. Mashanovich, and I. Molina-Fernández, "Mid-infrared suspended waveguide platform and building blocks," IET Optoelectronics **13**, 55–61 (2019).
20. R. Zheng, D. Gao, and J. Dong, "Ultra-compact broadband tunable graphene plasmonic multimode interferometer," IEEE Photonics Technol. Lett. **28**, 645–648 (2016).
21. C.-C. Huang and T.-C. Sun, "Numerical simulations of tunable ultrashort power splitters based on slotted multimode interference couplers," Sci. Reports **9**, 12756 (2019).
22. P. Cheben, R. Halir, J. H. Schmid, H. A. Atwater, and D. R. Smith, "Subwavelength integrated photonics," Nature **560**, 565–572 (2018).
23. R. Halir, A. Ortega-Moñux, D. Benedikovic, G. Z. Mashanovich, J. G. Wangüemert-Pérez, J. H. Schmid, I. Molina-Fernández, and P. Cheben, "Subwavelength-grating metamaterial structures for silicon photonic devices," Proc. IEEE **106**, 2144–2157 (2018).
24. R. Fernández de Cabo, D. González-Andrade, P. Cheben, and A. V. Velasco, "High-performance on-chip silicon beamsplitter based on subwavelength metamaterials for enhanced fabrication tolerance," Nanomaterials **11** (2021).
25. B. Dong, T. Hu, X. Luo, Y. Chang, X. Guo, H. Wang, D.-L. Kwong, G.-Q. Lo, and C. Lee, "Wavelength-flattened directional coupler based mid-infrared chemical sensor using bragg wavelength in subwavelength grating structure," Nanomaterials **8**, 893 (2018).
26. A. Herrero-Bermello, J. M. Luque-González, A. V. Velasco, A. Ortega-Moñux, P. Cheben, and R. Halir, "Design of a broadband polarization splitter based on anisotropy-engineered tilted subwavelength gratings," IEEE Photonics J. **11**, 1–8 (2019).
27. T. Hu, M. S. Rouifed, H. Qiu, X. Guo, C. G. Littlejohns, C. Liu, and H. Wang, "A polarization splitter and rotator based on a partially etched grating-assisted coupler," IEEE Photonics Technol. Lett. **28**, 911–914 (2016).
28. A. Ortega-Moñux, C. Alonso-Ramos, A. Maese-Novo, R. Halir, L. Zavargo-Peche, D. Pérez-Galacho, I. Molina-Fernández, J. G. Wangüemert-Pérez, P. Cheben, J. H. Schmid, J. Lapointe, D. Xu, and S. Janz, "An ultra-compact multimode interference coupler with a subwavelength grating slot," Laser & Photonics Rev. **7**, L12–L15 (2013).
29. R. Halir, P. Cheben, J. M. Luque-González, J. D. Sarmiento-Merenguel, J. H. Schmid, G. Wangüemert-Pérez, D.-X. Xu, S. Wang, A. Ortega-Moñux, and Í. Molina-Fernández, "Ultra-broadband nanophotonic beamsplitter using an anisotropic sub-wavelength metamaterial," Laser & Photonics Rev. **10**, 1039–1046 (2016).
30. M. A. Tran, T. Komljenovic, J. C. Hulme, M. L. Davenport, and J. E. Bowers, "A robust method for characterization of optical waveguides and couplers," IEEE Photonics Technol. Lett. **28**, 1517–1520 (2016).
31. T. Barwicz, B. Peng, R. Leidy, A. Janta-Polczynski, T. Houghton, M. Khater, S. Kamapurkar, S. Engelmann, P. Fortier, N. Boyer, and W. M. J. Green, "Integrated metamaterial interfaces for self-aligned fibre-to-chip coupling in volume manufacturing," IEEE J. Sel. Top. Quantum Electron. **25** (2019).